Observation and Estimation of Lagrangian, Stokes, and Eulerian Currents Induced by Wind and Waves at the Sea Surface

FABRICE ARDHUIN

Service Hydrographique et Océanographique de la Marine, Brest, France

LOUIS MARIÉ

Laboratoire de Physique des Océans, UM 6523 CNRS/IFREMER/IRD/UBO, Brest, France

NICOLAS RASCLE*

Laboratoire d'Oceanographie Spatiale, IFREMER, Brest, France

PHILIPPE FORGET

LSEET, Université du Sud Toulon-Var, CNRS (UMR6017), La Garde CEDEX, France

ARON ROLAND

Institut fur Wasserbau und Wasserwirtschaft, Technische Universitat Darmstadt, Darmstadt, Germany

(Manuscript received 24 October 2008, in final form 2 April 2009)

ABSTRACT

The surface current response to winds is analyzed in a 2-yr time series of a 12-MHz (HF) Wellen Radar (WERA) off the west coast of France. Consistent with previous observations, the measured currents, after filtering tides, are on the order of 1.0%–1.8% of the wind speed, in a direction 10°–40° to the right of the wind, and with systematic trends as a function of wind speed. This Lagrangian current can be decomposed as the vector sum of a quasi-Eulerian current $\mathbf{U}_E$, representative of the top 1 m of the water column and part of the wave-induced Stokes drift $\mathbf{U}_{ss}$ at the sea surface. Here, $\mathbf{U}_{ss}$ is estimated with an accurate numerical wave model using a novel parameterization of wave dissipation processes. Using both observed and modeled wave spectra, $\mathbf{U}_{ss}$ is found to be very well approximated by a simple function of the wind speed and significant wave height, generally increasing quadratically with the wind speed. Focusing on a site located 100 km from the mainland, the wave-induced contribution of $\mathbf{U}_{ss}$ to the radar measurement has an estimated magnitude of 0.6%–1.3% of the wind speed, in the wind direction—a percentage that increases with wind speed. The difference $\mathbf{U}_E$ of Lagrangian and Stokes contributions is found to be on the order of 0.4%–0.8% of the wind speed and 45°–70° to the right of the wind. This relatively weak, quasi-Eulerian current with a large deflection angle is interpreted as evidence of strong near-surface mixing, likely related to breaking waves and/or Langmuir circulations. Summer stratification tends to increase the $\mathbf{U}_E$ response by up to a factor of 2 on average, and further increase the deflection angle of $\mathbf{U}_E$ by 5°–10°. At locations closer to the coast, $\mathbf{U}_{ss}$ is smaller and $\mathbf{U}_E$ is larger with a smaller deflection angle. These results would be transposable to the World Ocean if the relative part of geostrophic currents in $\mathbf{U}_E$ was weak, which is expected. This decomposition into Stokes drift and quasi-Eulerian current is most important for the estimation of energy fluxes to the Ekman layer.

1. Introduction

Surface drift constitutes one of the most important applications of the emerging operational oceanography systems (e.g., Hackett et al. 2006), because it plays an important role in the fate of oil pollutions and larvae recruitment. A quantitative understanding of the relative

* Current affiliation: University of Cape Town, Rondebosch, South Africa.

Corresponding author address: Fabrice Ardhuin, Service Hydrographique et Océanographique de la Marine, 29609 Brest, France.
E-mail: ardhuin@shom.fr

DOI: 10.1175/2009JPO4169.1

contribution of the wave-induced Stokes drift to the near-surface velocities is also paramount for the proper estimation of air–sea energy fluxes (Kantha et al. 2009). The quantitative variation of surface drift as a function of the forcing parameters is still relatively poorly known. In areas of strong currents resulting from tides or quasi-geostrophic dynamics, the surface drift current is highly correlated to the subsurface current. Otherwise, winds play a major role in defining the surface velocities.

Recent theoretical and numerical works (Ardhuin et al. 2004; Kantha and Clayson 2004; Rascle et al. 2006; Ardhuin et al. 2008b) have sought to reconcile historical measurements of Eulerian and Lagrangian (i.e., drift) velocities with recent knowledge on wave-induced mixing (Agrawal et al. 1992) and wave-induced drift (Rascle et al. 2008). These suggest that the surface Stokes drift U_{ss} induced by waves typically accounts for $\frac{2}{3}$ of the surface wind-induced drift, in the open ocean, and that the surface wind-related Lagrangian velocity $U_L(z)$ is the sum of the strongly sheared Stokes drift $U_S(z)$ and a relatively uniform quasi-Eulerian current $\hat{u}(z)$, defined by Jenkins (1987) and generalized by Ardhuin et al. (2008b). The Stokes drift decays rapidly away from the surface on a scale that is the Stokes depth D_S. For deep-water monochromatic waves of wavelength L, we take $D_S = L/4$, by analogy with the usual definition of the (2 times larger) depth of wave influence for the orbital motion (e.g., Kinsman 1965); that is, at that depth, the Stokes drift is reduced to 4% of its surface value. For random waves, a similar result requires a more complex definition, but the approximate same result can be obtained by using the mean wavelength $L_{03} = gT_{m03}^2$, where T_{m03} is the mean period defined from the third moment of the wave frequency spectrum (see appendix C). Smaller values, such as $L/(4\pi)$, which was used by Polton et al. (2005), are more representative of the depth where the Stokes drift is truly significant.

For horizontally homogeneous conditions, the depth-integrated quasi-Eulerian mass transport vector $\mathbf{M}^m$ is constrained by the balance between the Coriolis force and the wind stress τ_a and bottom stress τ_b (Hasselmann 1970; Ardhuin et al. 2004; Smith 2006):

$$\frac{\partial \mathbf{M}^m}{\partial t} + (\mathbf{M}^m + \mathbf{M}^w) \times f\mathbf{e}_z = \tau_a - \tau_b, \qquad (1)$$

where $\mathbf{M}^w$ is the (Stokes) mass "transport"[1] induced by surface gravity waves; f is 2 times the vertical component of the earth rotation vector, usually called the Coriolis parameter; and $\mathbf{e}_z$ is the vertical unit vector, which points up. The surface stress vector τ_a is typically on the order of $\rho_a C_d U_{10}^2$, where ρ_a is the air density, C_d is in the range $1–2 \times 10^{-3}$, and U_{10} the wind speed at 10-m height. The horizontal homogeneity is obviously never achieved strictly (e.g., Pollard 1983); this aspect will be further discussed in the context of our measurements.

The wind-driven current is not expected to be significant at a depth greater than 0.7 times the Ekman depth, $D_E = 0.4\sqrt{(\tau_a/\rho_w)}/f$ (i.e., less than 0.2% of the wind speed if the surface value is 2.8% of U_{10}; Madsen 1977). For a wind speed $U_{10} = 10$ m s^{-1}, $0.7D_E$ is on the order of 30 m. In locations with a larger water depth, the bottom stress is thus expected to be negligible. Further, this depth of maximum influence can also be limited by a vertical stratification, with larger velocities in shallow mixed layers and directions of U_E more strongly deflected to the right of the wind (in the Northern Hemisphere) than previously expected (Price and Sundermeyer 1999; Rascle 2007). It has also been proposed by Polton et al. (2005) that the wave-induced mass "transport" $\mathbf{M}^w$ may play a role in the modification of near-surface currents, but $\mathbf{M}^w$ is generally less than 30% of the Ekman transport $\mathbf{M}^E = \tau_a/f$, and its effect appears to be secondary compared to the stratification (Rascle and Ardhuin 2009). The time-averaged balance given by (1) is thus, approximately, $\mathbf{M}^m = -\mathbf{M}^w + (\tau_a \times \mathbf{e}_z)/f$. This was nearly verified for the Long-Term Upper Ocean Study (LOTUS3) dataset (Price and Sundermeyer 1999) when allowing for wave-induced biases in the mooring measurements (Rascle and Ardhuin 2009). Yet, this is not always the case (e.g., Nerheim and Stigebrandt 2006), possibly because of baroclinic currents and other phenomena that are difficult to separate from the wind-driven component.

The vertical profile of the quasi-Eulerian current is, under the same homogeneous and stationary circumstances, the solution of (Xu and Bowen 1994; Ardhuin et al. 2008b)

$$\frac{\partial \hat{\mathbf{u}}}{\partial t} + (\hat{\mathbf{u}} + \mathbf{u}_S) \times f\mathbf{e}_z = \frac{\partial}{\partial z}\left(K\frac{\partial \hat{\mathbf{u}}}{\partial z}\right), \qquad (2)$$

where K is a turbulent mixing coefficient.

These predictions were verified by Rascle (2007) with mooring data at depths greater than 5 m and surface-following measurements by Santala and Terray (1992) at depths larger than 2 m. When extrapolated to the surface using a simple numerical model, these observations give directions of U_E between 45° and 90°, more than the 45° given by the constant eddy-viscosity model of Ekman (1905), as extended by Gonella (1971), and the 10° given by the linear eddy-viscosity model of Madsen (1977). This surface angle, as well as the magnitude of U_E, is also critical for the estimation of the flux of wind energy

[1] Because the term $\mathbf{M}^w$ in the momentum balance (1) drives a component of mean transport that opposes M^w, there is no net wave-induced transport, except in nonstationary or nonhomogenous conditions (Hasselmann 1970; Xu and Bowen 1994).

to the Ekman layer (e.g., Wang and Huang 2004) or the analysis of near-surface drifter data (e.g., Rio and Hernandez 2003; Elipot and Lumpkin 2008). For a better understanding of these questions, it is thus necessary to use ocean velocities measured much closer to the surface.

High-frequency (HF) radars can provide such measurements at depths that depend on their operating frequency. Using a 30-MHz radar, Mao and Heron (2008) made observations that are also consistent with the idea that the drift current, found to be 2.1% of the wind speed on average, is the sum of U_E, which—according to their theory—depends quadratically on the wind speed, and U_{ss}, which they estimate to depend linearly on the wind speed, with a variation according to the fetch. Unfortunately, their analysis relied on empirical wave estimates that give large relative errors (on the order of 100%; see, e.g., Kahma and Calkoen 1992; Ardhuin et al. 2007) and a limited range of wind speeds. Other HF radar observations give a surface current on the order of 1.5%–2.5% of U_{10} (Essen 1993) with 25–30-MHz radars. Dobson et al. (1989) also report a ratio of 2.0% using a 22 MHz radar, and Shay et al. (2007) report a ratio of 2%–3% using a 16-MHz radar in water depths of 20–50 m. These analyses are difficult to interpret because of the filters applied on time series to remove motions (tides, geostrophic currents, etc.) that are not related to the wind and also because of the importance of inertial oscillations that make the wind- and wave-driven current a function of the full wind history and not just a function of the wind vector at the same time and location.

In the present paper, we extend the previous analyses of HF radar data by independently estimating the Stokes drift by using an accurate wave model. We find that, at our deep-water[2] northeast Atlantic site, the quasi-Eulerian current U_E is on the order of 0.6% of the wind speed with a direction that is, on average, 60° to the right of the wind. We also find that the time-dependent response of surface current to the wind is typical of a slab layer with a transfer function proportional to $1/(f + \omega)$, where ω is the radian frequency considered. This result is expected to be representative of the open ocean. Therefore, the estimates of the flux of wind energy to the Ekman layer by Wang and Huang (2004) and others may not be quantitatively correct: they used an angle of 45°, a surface velocity that is $2\sqrt{\tau_a/\rho_w}$ for steady winds (about 0.2% of the wind speed), and a transfer function proportional to $1/\sqrt{f + \omega}$. A proper analysis of the effects of waves is needed to properly evaluate energy fluxes.

Our new data and its processing are described in section 2. The analysis of the stratification effect is presented in section 3, with conclusions in section 4.

2. Lagrangian and quasi-Eulerian current from HF radars

a. Radar measurements and processing

High-frequency radars measure, among other things (e.g., Ivonin et al. 2004), the phase velocity **C** of Bragg waves that have a wavelength equal to one-half of the radar electromagnetic wavelength and propagate in directions away from and toward the radar. This phase velocity is a combination of the quasi-Eulerian current U_E (Stewart and Joy 1974; Kirby and Chen 1989), the phase speed of linear waves $C_{\rm lin}$, and a nonlinear wave correction (Weber and Barrick 1977) that can be interpreted as a filtered surface Stokes drift U_{Sf}. For monostatic systems, the usual radial current velocity in the direction θ_B toward one radar can be expressed as

$$\begin{aligned} U_R(\theta_B) &= C(\theta_B) - \mathbf{C}_{\rm lin} \cdot \mathbf{e}_{\theta_B}, \\ &= U_{Sf}(\theta_B) + \mathbf{U}_E \cdot \mathbf{e}_{\theta_B}, \end{aligned} \tag{3}$$

where $\mathbf{e}_{\theta_B}$ is the unit vector in direction θ_B. This velocity can be loosely interpreted as the projection in direction θ_B of a current vector $\mathbf{U}_R$. The reason why this is not exactly true is that $U_{Sf}(\theta_B)$ for all directions cannot be exactly given by the projection of a vector $\mathbf{U}_{Sf}$. In other words, $U_{Sf}(\theta_B)$ is not exactly proportional to $\cos(\theta_B)$, although it is a reasonable approximation (Broche et al. 1983).

To express U_{Sf}, we first define the Stokes drift vector for waves with frequencies up to f_c from the directional wave spectrum $E(f, \theta)$:

$$\mathbf{U}_{\rm ss}(f_c) = 4\pi \int_0^{f_c} \int_0^{2\pi} f\mathbf{k}(f,\theta)E(f,\theta)\, df\, d\theta, \tag{4}$$

where $k(f)$ is the magnitude of the wavenumber **k**, which is equal to $(2\pi f)^2/g$ for linear waves in deep water, and g is the acceleration of gravity. Starting from the full expression given by Weber and Barrick (1977), Broche et al. (1983) showed that the filtered Stokes drift component that affects the radial current measured by one radar station is well approximated by

$$\begin{aligned} U_{Sf}(k_B,\theta_B) \simeq\ & \mathbf{U}_{\rm ss}(f_B) \cdot \mathbf{e}_{\theta_B} \\ & + 4\pi k_B \int_{f_B}^{\infty} \int_0^{2\pi} f\cos(\theta - \theta_B)E(f,\theta)\, d\theta\, df, \end{aligned} \tag{5}$$

where f_B is the frequency of the Bragg waves and $\mathbf{k}_B$ is the corresponding wavenumber vector, with a direction

[2] This means deeper than both the Stokes depth D_S and the expected Ekman depth D_E.

θ_B and magnitude k_B. The full expression, correcting typographic errors in Broche et al. (1983) is given in appendix A. To simplify the notations, the variable k_B in U_{Sf} will now be omitted, but the filtered Stokes drift is always a function of the Bragg wavenumber, thus being different for different radar frequencies.

The depth-varying quasi-Eulerian current $\hat{\boldsymbol{u}}(z)$ is defined as the difference of the Lagrangian velocity and Stokes drift (Jenkins 1987) and can generally be estimated from the full velocity field using a generalized Lagrangian mean (Ardhuin et al. 2008b). The value $\mathbf{U}_E$ estimated from the radar is, according to linear wave theory, the integral of $\hat{\boldsymbol{u}}(z)$ weighted by the Bragg wave Stokes drift profile (Stewart and Joy 1974; Kirby and Chen 1989). In deep water, this is

$$\mathbf{U}_E = 2k_B \mathbf{e}_{\theta_B} \cdot \int_{-\infty}^{0} \hat{\mathbf{u}} \exp(2k_B z)\, dz. \tag{6}$$

Here, we use data from an HF Wellen radar (WERA) system (Gurgel et al. 1999), which is manufactured by Helzel GmbH and operated at 12.4 MHz. The Bragg wavelength is 12.1 m, corresponding to a wave frequency of 0.36 Hz in deep water. Thus, half of the weight $\exp(2k_B z)$ in Eq. (6) comes from water depths less than 0.6 m from the moving sea surface, compared to 0.28 m with the 30-MHz radar of Mao and Heron (2008). The relative contributions from deeper layers to U_E decrease exponentially with depth as $\exp(2k_B z)$. Therefore, U_E can be interpreted as the quasi-Eulerian current in the top 1 m of the ocean.

The radar system has been deployed and operated by Actimar SAS since July 2006 on the west coast of France (Fig. 1), measuring surface currents and sea states every 20 min. The area is characterized by intense tidal currents, in particular between the largest islands where it exceeds 3 m s^{-1} during mean spring tides. Also important, the offshore stratification is largely suppressed by mixing due to the currents in the areas shallower than 90 m, resulting in complex temperature fronts that are related to the bottom topography (e.g., Mariette and Le Cann 1985).

Each radar station transmits a chirped continuous wave with a repetition frequency of 4 Hz and a 100-kHz bandwidth, which gives a radial resolution of 1.5 km. The receiving antennas are 16-element linear arrays with a spacing of 10 m, giving a typical angular resolution of 15°. The raw data are processed to remove most of the interference signals (Gurgel and Barbin 2008). Ensemble averaging over 4 consecutive segments of 512 pulses yields a velocity resolution $d_u = 0.09$ m s^{-1} in the Doppler spectrum used to estimate each individual radial current measurement. Yet, the current value is obtained by a weighted sum over a 9-point window applied to the Doppler spectrum. Provided that some inhomogeneity exists in the current field, the width of the Doppler spectrum permits a measurement resolution that is infinitely small but with an accuracy that is difficult to define, because no other instrument, except maybe for the Coastal Dynamics Experiment (CODE)-type drifter (Davis 1985), is able to measure surface current in the top 1 m of the ocean. Similarly, satellite altimeters are reported to measure the mean sea level position with an accuracy on the order of 2 cm, whereas their typical range resolution is close to 40 cm. Prandle (1987) used the coherence of the tidal motions to infer that the accuracy of his 27-MHz radar system was indeed less than the Doppler resolution when averaged over one hour. We will thus take the accuracy to be equal to the resolution; however, as it appears later in this paper, the only source of concern for our analysis is not so much the random error but a systematic bias, because we will average a very large number of independent measurements.

Because we investigate the relationship between surface currents and winds based on modeled winds and waves, we will consider only the temporal evolution of the wave field at one point of the radars' field of view that is representative of the offshore conditions, at a distance of 80–100 km from shore and with a water depth of 120 m. The reason for choosing this location is that we have verified the wind and wave model results to be most accurate offshore, where they were verified in situ with measurements that only span 6 and 9 months of our radar time series. Other reasons for looking at offshore conditions are the expected limited effect of the bottom and the expected small horizontal gradients of both tidal currents and other processes; that is, we stay away from the thermal front that typically follows the 90-m depth contour (Mariette and Le Cann 1985; Le Boyer et al. 2009). The downside of this choice is that the HF-derived current is generally less accurate as the distance from the coast increases, and the coverage is not permanent, especially during severe storms (e.g., Figure 1). These two drawbacks are limited in practice, as we now discuss.

Interferences and ships cause some data to be rejected in the radar processing or yield bad measurements, and heavy seas or calm seas also reduce the radar working range. To obtain a nearly continuous time series, we compiled and filtered data from a 0.2° latitude by 0.3° longitude box around that point (A in Fig. 1, with the arrow spacing indicating the resolution of the radar grid). This compilation was done in two steps. First, based on a visual inspection of the data, at each radar grid point, 0.05% of the total number of data points in the radial velocities time series are considered spurious and removed. These points are selected as the points where the raw radial current time series differs most

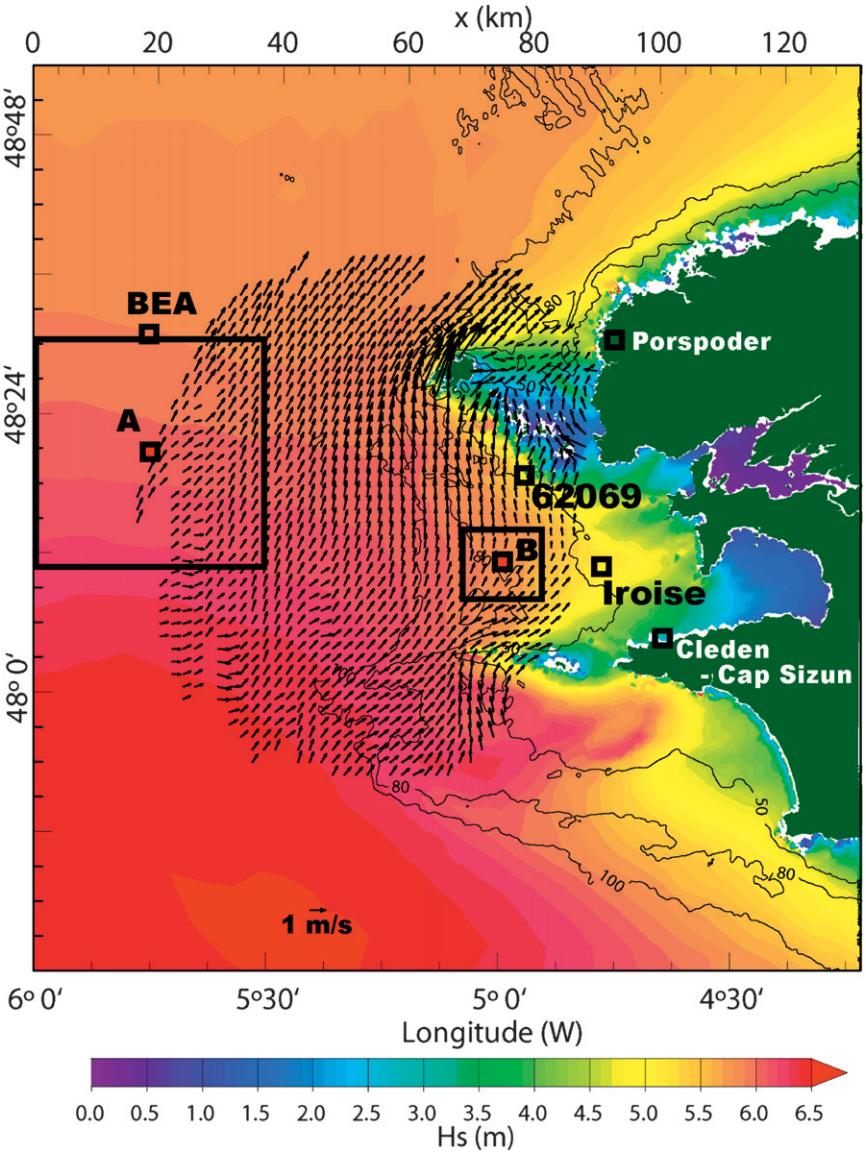

FIG. 1. Map of the area showing significant wave height at 1200 UTC 1 Jan 2008 estimated with a numerical wave model (see appendix B) and the instantaneous surface current measured by the HF radars installed at Porspoder and Cléden-Cap-Sizun, France. In situ measurement stations include the weather buoy Beatrice (number 62052); the Pierre Noires (62069) directional Datawell waverider buoy (installed from November 2005 to March 2006 and back again since January 2008); and a previous waverider deployment (Iroise), which is more representative of the offshore wave conditions. The large black square around point A is the area over which the radar data have been compiled to provide the time series analyzed here, which is representative of offshore conditions. When the radar functioned, measurements are available over the entire square for more than 80% of the 20-min records, a number than rises to 99% for the area east of 5°35′W. The partial radar coverage around point A is typical of high sea states with $H_s > 6$ m offshore, which are rare events.

from the result of a 5-point median filter. The 0.05% value was selected as a convenient rule of thumb, which removes most of the visibly spurious points but does not introduce too many unnecessary gaps in the time series. Second, the time series of all the grid points in the box around A were converted to u and v components and then averaged.

The Cartesian components of $\mathbf{U}_R$ and $\mathbf{U}_E$ with respect to west–east (u) and south–north (v) directions are calculated from the two radial components $U_R(\theta_{B1})$ and

$U_R(\theta_{B2})$, each measured by one radar station, before and after the subtraction of $\mathbf{U}_{Sf}(\theta_B)$. These Cartesian components suffer from a geometrical dilution of precision (GDOP) varying with position (Chapman et al. 1997; Shay et al. 2007). The radar beams intersect at point A with an angle $r = 34°$, and it is possible to estimate the GDOP values for u and v (i.e., the ratios S_u/s and S_v/s, where S_u, S_v, and S are the uncertainties in u, v, and u_r, respectively). Assuming that S has no bias and is uniformly distributed from $-d_u/2$ to $+d_u/2$, each radar measurement has intrinsic uncertainties $S_u = 0.04$ m s^{-1} and $S_v = 0.11$ m s^{-1}.

This compiled time series, extending from 5 July 2006 to 31 July 2008, is the basis of the following analysis. The 1200-s resolution data were averaged over 3-h blocks centered on round hours. Gaps shorter than 6 h were linearly interpolated. That time series is 97% complete and thus covers two full years. Other parts of the radar field of view yield similar results, briefly discussed later. Because of averaging in space and time, each point in the time series is the combination of about 30 range cells and 9 time intervals (i.e., 180 independent velocity measurements when the full radar range is obtained). Even with an 11 cm s^{-1} uncertainty on the original measurement, the expected root-mean-square (rms) errors on the velocity components are thus less than 1 cm s^{-1}. This analysis assumes that the instrument is not biased. After verification of the radar antenna lobe patterns using both in situ transmitters and a novel technique based on the analysis of radio interference (to be described elsewhere), the main lobe of the radar is known to be mispointed by less than 5°, with a −3-dB width less than 15°. The largest source of uncertainty is thus the interpretation of the phase speed and the numerical estimation of the Stokes drift, as discussed later.

Because we wish to focus on the random wind-driven currents, we also performed a tidal analysis using the T-Tide software (Pawlowicz et al. 2002) applied to each velocity component. This analysis on the full time series (before time averaging) allows the removal of the deterministic diurnal constituents K_1, O_1, P_1, and Q_1 that have amplitudes of 1.5–0.3 cm s^{-1}, with estimated errors of 0.1 cm s^{-1}. Because this only corrects for 95% of the apparent variance in the M_2 and S_2 semidiurnal tides, these will be further filtered by using a time filter.

b. Numerical wave model and estimations of Stokes drift

1) General principles

As expressed by Eq. (5), the estimation of $U_{Sf}(\theta_B)$ requires the measurement or modeling of the wave spectrum $E(f, \theta)$. In situ buoys were moored for restricted periods at several locations for the investigation of offshore to coastal wave transformation (Ardhuin 2006) and to provide complementary data for radar validation. The radar also measures the sea state, but the coverage is often limited and its accuracy for a 20-min record is typically only on the order of 25% for the significant wave height H_s. Thus, to use the full current time series at the offshore location (point A), we have to estimate the sea state by using a numerical wave model.

We use an implementation of the WAVEWATCH III (WWIII) code, in its version 3.14 (Tolman 2007, 2008), with minor modifications of the parameterizations (see appendix B) and the addition of advection schemes on unstructured grids (Roland 2009).

The model setting consists of a two-way nested pair of grids, covering the global ocean at 0.5° resolution and the Bay of Biscay and English Channel at a resolution of 0.1°. A further zoom over the measurement area is done using an unstructured grid with 8429 wet points (Fig. 1). The model setting is fully described in appendix B.

In practice, U_{Sf} is dominated by the first term $U_{ss}(f_B)$, in Eq. (5). Examining a large number of spectral data (6 buoys for 2 yr spanning a range of wave climates; see appendix C), we realized that $U_{ss}(f_B)$ is essentially a function of the wind speed U_{10} and the wave height H_s. Although U_{10} explains typically only 50% of the variance of $U_{ss}(f)$ with $0.3 < f < 0.5$, U_{10} and H_s generally explain over 85% of the variance. This behavior of $U_{ss}(f)$ is similar to that of the fourth spectral moment, which is related to the surface mean square slope (Gourrion et al. 2002; Vandemark et al. 2004). The reason for this correlation is that the wind speed is obviously related to the high-frequency part of the wave spectrum, which determines most of the Stokes drift, whereas H_s is a surrogate variable for both the presence of swell and the stage of development of the wind sea. Here, we find

$$U_{ss}(f_c) \simeq 5.0 \times 10^{-4}\left[1.25 - 0.25\left(\frac{0.5}{f_c}\right)^{1.3}\right]U_{10} \times \min\{U_{10}, 14.5\} + 0.025(H_s - 0.4). \quad (7)$$

The relationship given by Eq. (7) appears to be very robust, with a 2.6 cm^{-1} rms difference compared to global hindcast values of $U_{ss}(\infty)$, which is a 16.9% difference. Nevertheless, when compared to buoy data, an accurate wave model generally provides a better fit to the observations (appendix C). We thus have used our hindcasts using WAVEWATCH III to provide an estimate for U_{Sf}.

2) Uncertainty on U_{SF} around point A

We have no wave measurement at point A and no permanent spectral measurement in the area. A detailed

validation of U_{ss} was thus performed for the coastal buoys 62069 (Fig. 1) and 62064 (off Cap Ferret, 600 km to the southeast of point A), the U.S. Northwest Pacific coast (appendix C), the U.S. East Coast, the Gulf of Mexico, and California.

We further use wave information at buoy 62163, located 150 km west of point A, which is representative of the offshore conditions found at point A and a combination of satellite altimeter data. The present model estimates of H_s are more accurate at buoy 62163, located 150 km west of point A, than at Pacific buoy locations. Further, the model estimate of the fourth moment m_4 of the wave spectrum is better correlated in the Bay of Biscay to radar altimeter C-band cross sections compared to other regions of the World Ocean (appendix C). We thus expect the model estimate of $U_{ss}(f_B = 0.36\ \text{Hz})$ to have a bias smaller than 5%, with a random error less than 20% (see appendix C). As a result, we chose to use this numerical wave model for the estimation of U_{ss} and U_{Sf}. We can thus propose an error budget for our estimate of the wind-driven quasi-Eulerian current in which the measurement error is dominated by U_{Sf} with a bias of 5% at most and a standard deviation less than 20% overall. Using the analysis of 2 yr of model results, this standard deviation at the Pacific buoy 46005 is 24% for wind speeds of 3 m s^{-1}, 20% for wind speeds of 5 m s^{-1}, 16% for wind speeds of 7 m s^{-1}, and 11% for wind speeds of 11 m s^{-1}. Given the general accuracy of the wave model in the northeast Atlantic, we expect similar results here.

We thus estimate that the root-mean-square error of the modeled quasi-Eulerian current U_E at 3-h intervals is on the order of 0.2% of U_{10}. On this time scale, it is difficult to rule out contributions from horizontal pressure gradients in the momentum balance, and this current may not be purely wind driven.

The averaged current (e.g., for a given class of wind speed, as shown in Fig. 7) has a relative accuracy better than 0.1% of U_{10}. In situ measurements of time-averaged velocities from 10 to 70 m above the bottom at 48°6′N, 5°23′W (south of point A; see Fig. 1) using an RD Instruments Workhorse acoustic Doppler current profiler (ADCP) deployed from June to September 2007 (Le Boyer et al. 2009) give tide-filtered currents less than 2 cm s^{-1} or 0.25% of the wind speed when averaged following the wind direction (the instantaneous measurements are rotated before averaging) and less than 0.1% when winds are stronger than 10 m s^{-1}. This is typically less than 20% of U_{Sf}. Assuming that wind-correlated baroclinic currents are negligible during the ADCP measurement campaign, the wind-correlated geostrophic current is expected to be less than 0.2% of U_{10}. Generalizing this result to the entire radar time series, the averaged values of U_E can be interpreted as a wind-driven current with an accuracy to within 0.3% of U_{10}.

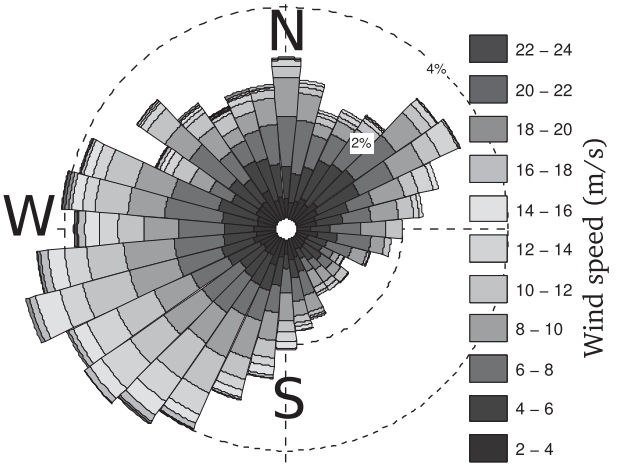

FIG. 2. Wind rose for the years 2006–08 at point A, based on ECMWF analyses. The observations at Beatrice buoy give a similar result. For each direction, the cumulative frequency is indicated with wind speeds increasing from the center to the outside, with a maximum of 4.3% maximum from west-southwest (heading 250°). An isotropic distribution would have a maximum of 2.7%.

3. Analysis of wind-driven flows

The study area is dominated by moderate 6–12 m s^{-1} winds, from a wide range of directions, with slightly dominant southwesterly and northeasterly sectors (Fig. 2).

a. Rotary spectral analysis

The rotary spectral analysis gives both the frequency distribution of the signal, and an indication of its circular polarization (Gonella 1971). The positive frequencies correspond to counterclockwise (CCW) motions, and the negative frequencies correspond to clockwise (CW) motions, the usual polarization of inertial motions in the Northern Hemisphere.

The instantaneous measurements of the radar are dominated by tidal currents, and the variance of motions with frequencies less than 1.75 counts per day (cpd) only accounts for 8% of the total variance (Fig. 3). These low frequency motions include the diurnal tidal constituents, most importantly K_1 and O_1, but these only account for 0.1% of the variance. The low frequency motions are generally dominated by near-inertial motions, which are polarized clockwise with frequencies close to the inertial frequency $f_I = 1.3$ cpd (see Fig. 3).

b. Cospectral analysis

Here, we investigate the relationship between measured currents (processed as described earlier) and winds

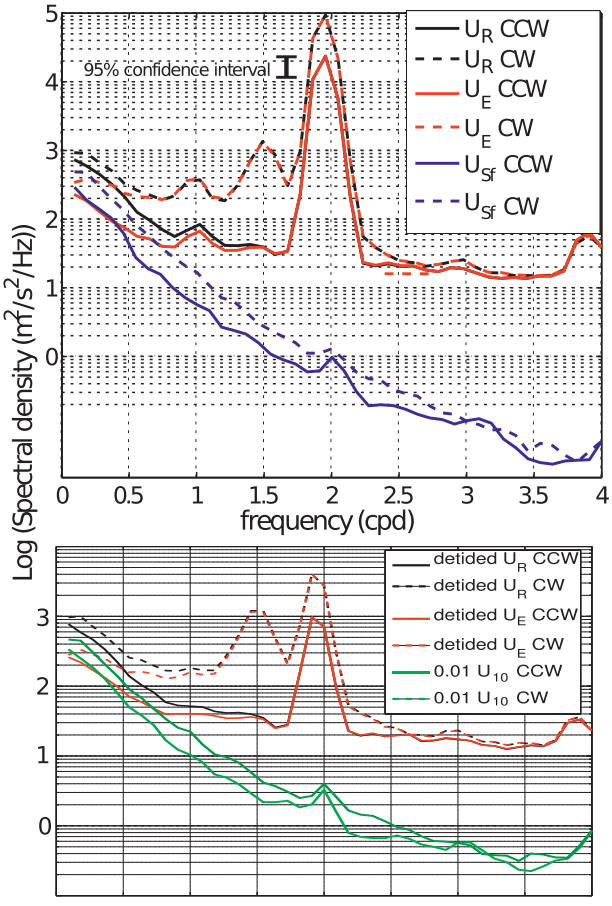

FIG. 3. Rotary power spectra of the current measured by the radar, and the contribution U_{Sf} to the surface Stokes drift estimated via Eq. (A1). CW motions are shown with dashed lines and CCW motions are shown with solid lines. The spectra were estimated using half-overlapping segments 264 h long over the parts of the time series with no gaps. The number of degrees of freedom is taken to be the number of nonoverlapping segments (e.g., 59 at the spectral resolution of 0.09 cpd, giving a relative error of 35% at the 95% confidence level). (bottom) The tidal components have been filtered out, which clearly removes the diurnal peak. However, the semidiurnal tides are only reduced by a factor of 25, which is not enough compared to the magnitude of the near-inertial motions and requires the use of an additional filter. This tide-filtered time series is used in all of the following analyses.

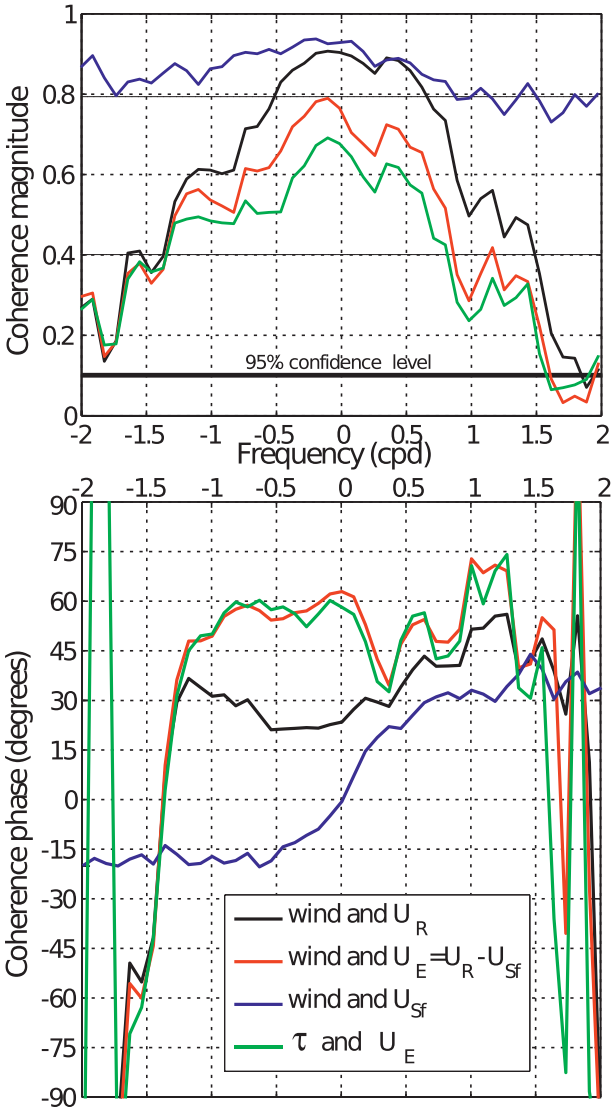

FIG. 4. (a) Magnitude and (b) phase of rotary cospectra of the wind and wind stress with the radar-derived current, Stokes drift, and Eulerian current. The number of degrees of freedom is 108 at the spectral resolution of 0.09 cpd. Coherence is significant at the 95% confidence level for a value of 0.1. Negative and positive frequencies are CW and counterclockwise polarized motions, respectively.

taken from 6-hourly wind analyses from the European Centre for Medium-Range Weather Forecasts (ECMWF). These analyses were verified to give excellent correlation ($r \simeq 0.92$) with the Beatrice buoy (WMO code 62052), which unfortunately malfunctionned during large periods of time. The wind and current data are thus completely independent. The wave model was forced by these same winds; thus, the high level of coherence between the predicted Stokes drift and the wind (Fig. 4) is not surprising.

To isolate the wind-correlated dynamics from the shorter (tide) and longer (general circulation) time scales, we first perform a cospectral analysis of the measured currents with the wind, following the method of Gonella (1971). To keep as many data as possible between data gaps, the Fourier transforms are taken over 264 h, which corresponds to 21 M_2 tidal cycles. The measured currents are significantly coherent with the wind vector over the range -1.75 to 1.75 cpd (Fig. 4). This coherence is generally reduced when the Stokes component U_{Sf} is subtracted from the radar measurements.

The radar-measured current vectors $\mathbf{U}_R$ have stable directions relative to the wind, 20°–40° to the right for $f > -f_I$, given by their coherence phase (Fig. 4). The coherence phase of the Stokes drift increases with frequency. This pattern is typical of a time lag that can be estimated to about 1.5 h, which is consistent with the relatively slow response of the wave field compared to the current. This is rather short compared to the time scale of wave development, but one should bear in mind that the Stokes drift is mostly due to short waves that respond faster to the wind forcing than the dominant waves. Because the wind preferentially turns clockwise, the Stokes drift is slightly to the left of the wind. The asymmetry in the phase of U_{Sf} for clockwise and counterclockwise motions may be related to varying fetch when the wind turns.

As expected from the theory by Gonella (1972), the phase of the quasi-Eulerian current U_E jumps by about 180° at the inertial frequency $-f_I$. In the frequency range from −1.2 to 0.2 cpd, which contains 40% of the nontidal signal, U_E is at an angle between 45° and 60° to the right of the wind. This conclusion is not much altered when one correlates the Eulerian current against the wind stress, which for simplicity is estimated here with a constant drag coefficient $\boldsymbol{\tau} = \rho_a 1.3 \times 10^{-3} \mathbf{U}_{10} U_{10}$, where ρ_a is the air density. One may argue that the theoretical filtering of the Stokes drift is not well validated. A lower bound on the estimate of U_{Sf} can be given by removing the contribution from waves shorter than the Bragg waves. This has very little impact on the estimation of U_E.

The observed coherence phases of U_E and U_{10} are similar to the values given by Gonella (1972, Fig. 6), which are based on the constant eddy-viscosity model of Ekman (1905), but for the current considered at a depth as large as 25% of the Ekman depth. Because the radar measurements are representative of the upper 1 m and the Ekman depth is generally on the order of 30 m, it follows that the classical Ekman theory, with a constant eddy viscosity, does not apply here. Instead, this large near-surface deflection is consistent with model results obtained with a high surface mixing—such as those induced by Langmuir circulations (McWilliams et al. 1997; Kantha and Clayson 2004), breaking waves (Craig and Banner 1994; Mellor and Blumberg 2004; Rascle et al. 2006), or both—and consistent with the few observed near-surface velocity profiles (Santala and Terray 1992).

c. Effects of stratification

Following the theory of Gonella (1972) and the previous observations by Price and Sundermeyer (1999), it is expected that the stratification has a significant effect on the surface currents. Here, we used sea surface temperature time series to diagnose the presence of a stratification. Because of the strong vertical mixing year round at the site of buoy 62069, the horizontal temperature difference between point A and point 62069 is a good indicator of the vertical stratification at point A. This temperature difference reaches up to 2°C and was present in 2006, 2007, and 2008 from early July to late October, as revealed by satellite SST data. We thus separated the data records used for the spectral analysis into ''stratified'' and ''homogeneous'' records based on the date of the midpoint in these time series.

These two series show a significant difference (at the 95% confidence level) when the spectra are smoothed over 0.3-cpd bands, with a 2 times larger response in the cases expected to be stratified (dashed lines, Fig. 5) for frequencies in the range of −1.7 to 1.5 cpd. Additionally, the current variance in the frequency band $-1.7 < f <$ 1.3 cpd exhibits a pronounced annual cycle, with a maximum in July or August at 6–7 times the January minimum, despite weaker winds (not shown). Interestingly, the transfer functions decrease like $1/(f + \omega)$ from a peak at the inertial frequency f, where ω is the radian frequency. This decrease is typical of slab-like behaviors that are expected in mixed layers with a much larger surface mixing (e.g., Rascle et al. 2006) than typically used with Ekman theory or a mixed-layer depth much shallower than the Ekman depth (Gonella 1972). Ekman theory in unstratified conditions, which should apply to our winter and spring measurements, would give a much slower decrease that is proportional to $1/\sqrt{(f + \omega)}$ (Gonella 1972). Together with this stronger amplitude of the current response in stratified conditions, we find a larger deflection angle in the −0.8 to −0.2-cpd frequency range. This pattern of larger currents and larger deflection angles in stratified conditions is consistent with the observations of Price and Sundermeyer (1999) and the numerical model results by Rascle and Ardhuin (2009).

d. Relationship between tide-filtered currents and winds

A proper model for the wind-induced current may be given by the relationship between the wind speed and wave height, giving the Stokes drift and the complex transfer function (transfer function and phase) from the wind stress spectrum to the Eulerian current spectrum, following Gonella (1971) or Millot and Crépon (1981). Such a model is beyond the scope of the present paper.

Simpler models that would give the current speed and direction as a function of the instantaneous wind vector are even less accurate. Because the transfer function is very peaked at the inertial frequency, the current speed may vary widely for a given wind speed. Yet, for practical reasons, there is a long tradition of directly comparing current and wind magnitudes and directions for

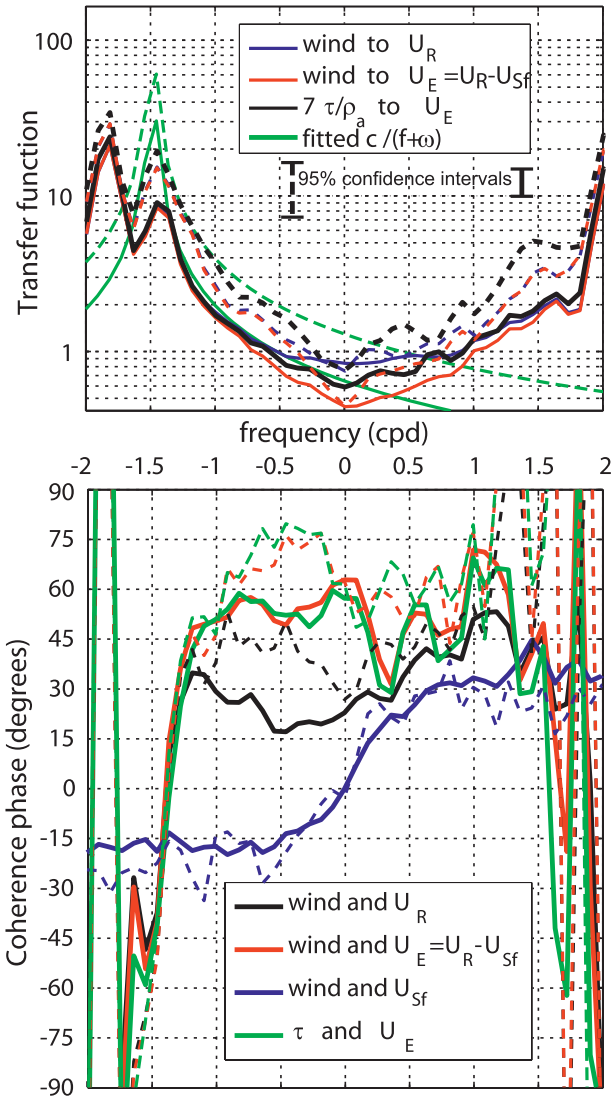

FIG. 5. Amplitude (top) transfer functions and (bottom) coherence phases between the wind forcing and the current response. The dashed lines correspond to records where a stratification is expected to be important (18 out of 108), and the solid lines correspond to the other records. Confidence intervals for the two groups of records are shown for the native spectral resolution of 0.09 cpd. To be at a comparable level, the wind stress was multiplied by 50 before estimating the transfer function. The two peaks of the transfer functions at ±2 cpd are due to the tidal currents but do not correspond to a causal relationship between the wind forcing and the current response.

search and rescue operations and ocean engineering applications. Because of the inertial oscillations, there is usually a large scatter in the correlation of the current and wind speed vectors. To compare with previous analyses (e.g., Mao and Heron 2008), we thus perform such a comparison after filtering out the dominant tidal current by taking the inverse Fourier transform of the current, wind, and Stokes drift spectra in which the amplitudes of components with frequencies higher than 1.75 cpd as well as the zero frequency are set to zero. Again, the Fourier transforms are taken over 264 h.

We find that the surface Eulerian U_E current lies 40°–60° to the right of the wind, suggesting that the near-inertial motions only add scatter to the longer period motions ($|f| < 1.3$ cpd) that were found to have similar deflection angles. Interestingly, the typical magnitude of U_E decreases from about 0.8% of U_{10} at low wind to nearly 0.4% for high winds. This reduction in the relative magnitude of U_E is accompanied by a reduction of the deflection angle from 65° on average for $U_{10} = 3$ m s^{-1} to 40° for $U_{10} = 15$ m s^{-1}. On the contrary, the Stokes drift typically increases quadratically with the wind speed. These observations contradict the usual theoretical statements of Kirwan et al. (1979) and Mao and Heron (2008); they concluded that the Stokes drift should be linear and the Eulerian current should be quadratic in terms of wind speed. The fact that the Stokes drift is quadratic as a function of the wind speed is shown by the fitted Eq. (7) (as well as observed wave spectra in Fig. C1). The error in Mao and Heron (2008) is likely due to their erroneous assumption that the Stokes drift is dominated by waves at the peak of the spectrum. In the analysis of Kirwan et al. (1979) and Rascle et al. (2006), the error essentially arises from the assumed shape of the wave spectrum.

The less-than-linear dependence of U_E on U_{10} contradicts the usual simple Ekman model for the quasi-Eulerian current, which would predict a current proportional to the wind stress and thus varying as the square or cube of the wind speed. This difference is likely due to the enhanced mixing caused by breaking waves, which tends to mix the momentum over a scale on the order of the wind–sea wave height (i.e., increasing with the wind speed; Terray et al. 1996; Rascle et al. 2006). Numerical models without stratification but with a realistic mixing tend to give a quasi-Eulerian current that increases with wind speed and with the inverse wave age. Here, the stronger winds do not correspond to very different wave ages, and it is likely that a correlation of deeper mixed layers with stronger winds is the cause of the reduction of U_E with increasing wind speed (Rascle and Ardhuin 2009). As a result, the nonlinear current response to the wind stress will likely limit the accuracy of models based on transfer functions.

e. Effects of fetch or wave development

The same analysis was also repeated for other points in the radar field of view; for example, at point B (Fig. 1), the radar data quality is generally better, but the wave model may have a bias of about 10% on U_{ss} and the

ECMWF wind field may be less accurate. Point B is relatively sheltered from southerly and northwesterly waves, and the fetch from the east is 40 km at most. If we assume that the winds are accurate at that site too, we find that the radar-derived current is weaker relative to the wind, with $\mathbf{U}_R/U_{10}$ typically smaller by 0.2% (a ~15% reduction) compared to point A. This appears to be due to a reduction in U_{Sf}, which is only partially compensated for by a small increase in U_E. This difference between points A and B nearly vanishes when only westerly wind situations are considered (defined by winds within 60° from the westerly direction).

4. Conclusions

Using a 2-yr time series of HF radar data and a novel numerical wave model that is shown to reproduce the observed variability of the surface Stokes drift with wind speed and wave height, we have analyzed the wind-driven surface current. When tidal currents are filtered out, theory predicts that the measured velocities are a superposition of a filtered Stokes drift U_{Sf} and a quasi-Eulerian current U_E. With our 12-MHz radar, U_{Sf} is estimated to be on the order of 0.5%–1.3% of the wind speed, with a percentage that increases linearly with wind speed. These values are a function of the radar wavelengths and would be larger, by up to 20%, with higher-frequency radars that give currents representative of a shallower surface layer. The other component U_E is found to be on the order of 0.6% of the wind speed and lies in our Northern Hemisphere at an average 40°–70° to the right of the wind, with a large scatter because of inertial oscillations that may be well modeled by using a Laplace transform of the wind stress (Broche et al. 1983). This large deflection angle is robustly given by the coherence phase for clockwise motions in the frequency range from 0 to the inertial frequency.

When instantaneous currents are compared to the wind, the magnitude of U_E appears to decrease with wind speed, but it increases when a stronger stratification is expected (Fig. 6). These surface observations correspond to currents in the depth range 0–1.6 m and confirm previous analysis of deeper subsurface mooring data. If wind-correlated geostrophic currents are negligible in our measurements, the shape of the classical picture of the Ekman spiral is not correct and the surface layer is much more slab-like than assumed in many analyses, probably because of the large wave-induced mixing at the surface (Agrawal et al. 1992). These findings are summarized in Fig. 7.

If we neglect the wind-correlated geostrophic currents, which we deem reasonable, and interpret U_E as being purely wind-driven, our observations of U_E/U_{10} at point A are expected to be representative of the open ocean, whereas in coastal areas and small basins, a less developed sea state will lead to a smaller U_{Sf} and a larger U_E, as we observe at point B. Such a generic relationship of U_E and U_{10} is very important for a proper estimation of the energy flux to the mixed layer. Besides, on top of the wind stress work on the Ekman current, this energy flux should be dominated by the dissipation of wave energy induced by breaking (e.g., Rascle et al. 2008). Also, there is the depth-integrated Stokes–Coriolis force that is equal to the product of the depth-integrated Stokes transport $\mathbf{M}^w = \rho_w \int \mathbf{U}_s(z)\, dz$

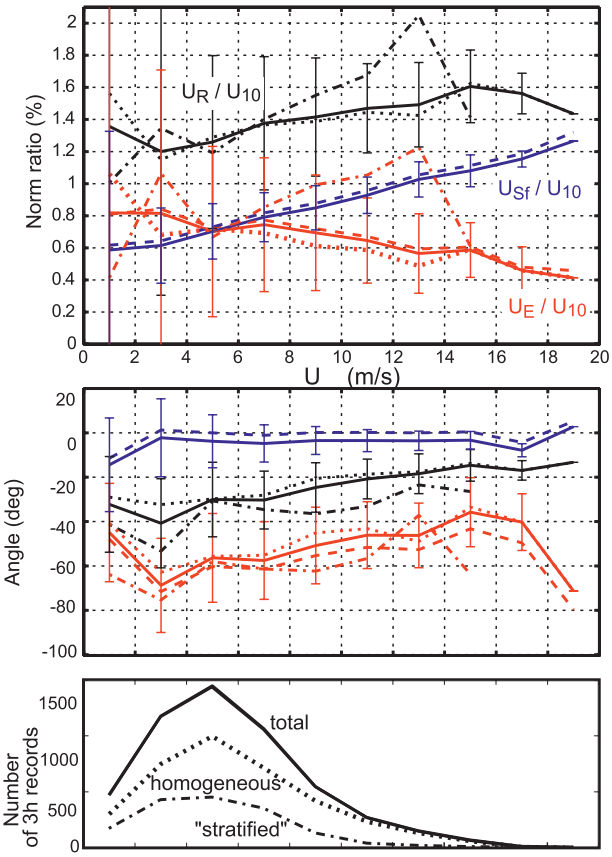

FIG. 6. Observed tide-filtered quasi-Eulerian velocity magnitudes normalized by the wind speed and directions relative to the wind vector. The linear increase of U_{Sf}/U_{10} with U_{10} is consistent with the quadratic dependence of U_{Sf} on U_{10} given by Eq. (7). The full dataset was binned according to wind speed. Dashed–dotted lines correspond to stratified conditions only and dotted lines correspond to homogeneous conditions. (bottom) The number of data records in each of these cases. The dashed line show results when U_{Sf} is replaced by $U_{ss}(f_B)$. Error bars show only 1/2 of the standard deviation for all conditions combined, in order to make the plots readable. All time series (wind, current, U_{Sf}, and U_{ss}) were filtered in the same manner for consistency (except for the initial detiding applied only to the current data). The error bars do not represent measurement errors but rather the geophysical variability due to inertial motions.

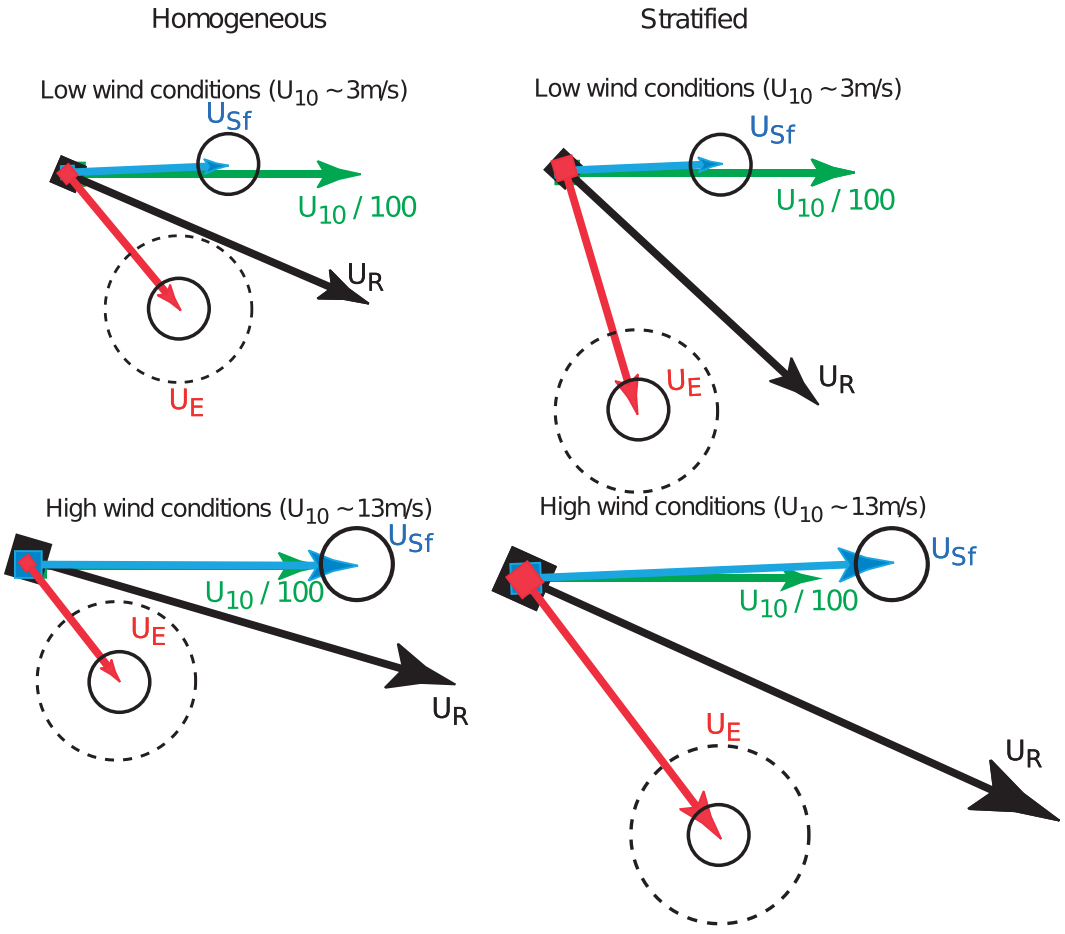

FIG. 7. Mean wind-correlated current vectors in low and high wind conditions, with and without stratification, measured off the west coast of France with the 12.4-MHz HF radar, based on the results shown in Fig. 6. Here, $\mathbf{U}_R$ is the radar-measured vector, which can be interpreted as a sum of a quasi-Eulerian current $\mathbf{U}_E$, representative of the upper 2 m and a filtered surface Stokes drift $\mathbf{U}_{Sf}$. The full surface Stokes drift is typically 40% larger than this filtered value. Solid circles give the expected error on the mean current components resulting from biases in the wave contribution to the radar measurement. The dashed circles show the expected error on the interpretation of U_E as a wind-driven current based on the ADCP measurements at depths of 60–120 m, assuming that the baroclinic part of the geostrophic current is negligible.

and the Coriolis parameter f. This force is smaller than the depth-integrated Coriolis force by about a factor of 3 on average (Rascle et al. 2008), but that may give a comparable work because of the smaller angle between that force and the quasi-Eulerian current $\hat{\mathbf{u}}(z)$. The accurate estimation of the surface Stokes drift using a numerical wave model also opens the way for a more accurate interpretation of space-borne measurements of surface currents using Doppler methods, which are contaminated by a Stokes-like component amplified 10 times or more (Chapron et al. 2005).

Acknowledgments. The efforts of Vincent Mariette and Nicolas Thomas are essential to maintain the radars in proper operating conditions. Funding for the radar purchase and maintenance was provided by DGA under the MOUTON project, and funding for the wave model development was provided under the ECORS project. Florent Birrien performed the integration of Aaron Roland's routines into the WAVEWATCH III framework. Wind and wave data were kindly provided by ECMWF, Météo-France, and the French Centre d'Etudes Techniques Maritimes Et Fluviales (CETMEF), and the sea surface temperature data used to diagnose the presence of a stratified layer were taken from the ODYSSEA Level 4 global analysis product, produced as part of the MERSEA Integrated Project. The SHOM buoy deployments were managed by David Corman with precious help from Guy Amis.

APPENDIX A

Nonlinear Correction for the Wave Dispersion Relation in a Random Sea State

Based on the lowest order approximate theory of Weber and Barrick (1977) for deep-water waves with $f \simeq 2\pi\sqrt{gk}$, the nonlinear correction to the phase speed of components with wavenumber k_B and direction θ_B can be expressed as an integral over the wave spectrum. Defining $x = k/k_B$ and $\alpha = \theta - \theta_B$, Broche et al. [1983, their Eq. (A2)] give the following expression:

$$U_{Sf}(k_B, \theta_B) = \frac{\sqrt{g}}{2} k_B^{3/2} \int_0^{\infty} \int_0^{2\pi} F(x, \alpha) E(f, \theta)\, d\theta\, df,$$

where, correcting for typographic errors and using $y = x^{1/2} = f/f_B$ and $a = \cos\alpha$,

$$F(x,\alpha) = y(2a - y + 3xa) + y \sum_{\varepsilon=\pm 1} \frac{\varepsilon - a}{a_\varepsilon - (1+\varepsilon y)^2} \{(ya - x)[a_\varepsilon + (1+\varepsilon y)^2]/2 + (1+\varepsilon y)[1 + \varepsilon xa + \varepsilon y(x + \varepsilon a) - a_\varepsilon]\}, \quad \text{(A1)}$$

with

$$a_\varepsilon = (1 + x^2 + 2\varepsilon xa)^{1/2}. \quad \text{(A2)}$$

These expressions give the correct figures in Broche et al. (1983). For $x < 1$, $F(x, 0) = 4x^{3/2}$; for $x > 1$, $F(x, 0) = 4x^{1/2}$ (Longuet-Higgins and Phillips 1962; Huang and Tung 1976; Barrick and Weber 1977). As commented by Broche et al. (1983), $F(x, \alpha) \simeq F(x, 0) \cos\alpha$, with the largest errors occurring for $x = 1$ where $F(x, \alpha) > F(x, 0) \cos\alpha$ for $|\alpha| < \pi/3$, which in our case makes U_{Sf} larger than the approximation given by Eq. (5) by 2%–5%.

APPENDIX B

Parameterization and Numerical Settings for the Wave Models

a. Parameterizations

The implementation of the WAVEWATCH III model used here was run with source functions S_{in}, S_{nl}, and S_{ds} parameterizing the wind input; nonlinear 4-wave interactions; and whitecapping dissipation. An extra additional dissipation term S_{db} is also included to enhance the dissipation resulting from wave breaking in shallow water, based on Battjes and Janssen (1978).

The parameterization for S_{nl} is taken from Hasselmann et al. (1985), with a minor reduction of the coupling coefficient from 2.78×10^7 to 2.5×10^7. The parameterizations for S_{in} and S_{ds} are very similar to the ones used by Ardhuin et al. (2008a), with modifications to further improve the high-frequency part of the spectrum (Filipot et al. 2008); that is, the whitecapping dissipation is based on recent observations of wave breaking statistics (Banner et al. 2000) and swell dissipation (Ardhuin et al. 2009). These model settings give the best estimates so far of wave heights, peaks, and mean periods but also of parameters related to the high-frequency tail of the spectrum (appendix C). The present model results are thus a significant improvement over the results of Bidlot et al. (2007) and Rascle et al. (2008). The physical and practical motivations for the parameterizations will be fully described elsewhere, and we only give here a description of their implementation. We only note for the interested users that the parameter settings given here tend to produce larger negative biases on H_s for $H_s > 8$ m than the parameterization by Bidlot et al. (2007). Better settings for H_s in extreme waves would be $s_u = 0$ and $c_3 = 0.5$ (see below), but this tends to give too large values of U_{ss}, which is why we do not use these settings here.

The parameterization of S_{in} is taken from Janssen (1991) as modified by Bidlot et al. (2007), with some further modifications for the high frequencies and the addition of a wind output term S_{out} (or "negative wind input") based on the observations by Ardhuin et al. (2009). The source term is thus

$$S_{\text{in}}(f,\theta) = \frac{\rho_a}{\rho_w} \frac{\beta_{\max}}{\kappa^2} e^Z Z^4 \left(\frac{u'_*}{C} + z_\alpha\right)^2 \times \cos^2(\theta - \theta_u)\sigma F(f,\theta) + S_{\text{out}}(f,\theta), \quad \text{(B1)}$$

where $\beta_{\max}$ is a (constant) nondimensional growth parameter; κ is the von Kármán constant; u_* is the friction velocity in the air; C is the phase speed of the waves, σ is the intrinsic frequency, which is equal to $2\pi f$ in the absence of currents; and $F(f, \theta)$ is the frequency-directional spectrum of the surface elevation variance. In the present implementation, the air–water density ratio is constant. We define $Z = \log(\mu)$, where μ is given by Janssen [1991, their Eq. (16)] and corrected for intermediate water depths, so that

$$Z = \log(kz_1) + \frac{\kappa}{[\cos(\theta - \theta_u)(u'_* + z_\alpha)]}, \quad \text{(B2)}$$

where z_1 is a roughness length modified by the wave-supported stress τ_w and z_α is a wave age tuning parameter. The effective roughness z_1 is implicitly defined by

$$U_{10} = \frac{u_*}{\kappa} \log\left(\frac{10\ \mathrm{m}}{z_1}\right), \tag{B3}$$

$$z_0 = \max\left\{\alpha_0 \frac{u_*^2}{g}, 0.0020\right\}, \quad \text{and} \tag{B4}$$

$$z_1 = \frac{z_0}{\sqrt{1-\tau_w/\tau}}, \tag{B5}$$

where τ is the wind stress magnitude, τ_w is the wave-supported fraction of the wind stress, U_{10} is the wind at 10-m height, and g is the acceleration of gravity.

The maximum value of z_0 was added to reduce the unrealistic stresses at high winds that are otherwise given by the standard parameterization. This is equivalent to setting a maximum wind drag coefficient of 2.8×10^{-3}. This and the use of an effective friction velocity $u'_*(f)$ instead of u_* in (B2) are the only changes to the general form of Janssen's (1991) wind input. That friction velocity is defined by

$$[u'_*(f)]^2 = \left| u_*^2 \mathbf{e}_\theta - |s_u| \int_0^f \int_0^{2\pi} \frac{S_{\mathrm{in}}(f',\theta')}{C} \mathrm{e}_{\theta'}\, df'\, d\theta' \right|. \tag{B6}$$

Here the empirical factor $s_u = 1.0$ adjusts the sheltering effect of short waves by long waves adapted from Chen and Belcher (2000) and helps to reduce the input at high frequency, without which a balance of source terms would not be possible (except with a very high dissipation as in Bidlot et al. 2007). This sheltering is also applied in the precomputed tables that give the wind stress as a function of U_{10} and τ_w/τ (Bidlot et al. 2007).

The wind output term is identical to the one used by Ardhuin et al. (2008a), based on the satellite observations of Ardhuin et al. (2009) with an adjustment to Pacific buoy data. Namely, defining the Reynolds number $\mathrm{Re} = 4u_{\mathrm{orb}}a_{\mathrm{orb}}/\nu_a$, where u_{orb} and a_{orb} are the significant surface orbital velocity and displacement amplitudes, respectively, and ν_a is the air viscosity, we take, for $\mathrm{Re} < 10^5$,

$$S_{\mathrm{out}}(f,\theta) = -1.2\frac{\rho_a}{\rho_w}(2k\sqrt{2\nu\sigma})F(f,\theta); \quad \text{otherwise,} \tag{B7}$$

$$S_{\mathrm{out}}(f,\theta) = -\frac{\rho_a}{\rho_w}(16 f_e \sigma^2 u_{\mathrm{orb}}/g)F(f,\theta), \tag{B8}$$

where

$$f_e = 0.7 f_{e,\mathrm{GM}} + [0.015 - 0.018\cos(\theta - \theta_u)]u_*/u_{\mathrm{orb}}. \tag{B9}$$

Here, $f_{e,\mathrm{GM}}$ is the friction factor given by Grant and Madsen's (1979) theory for rough oscillatory boundary layers without a mean flow, using a roughness length adjusted to 0.04 times the roughness for the wind. This gives a stronger dissipation for swells opposed to winds.

The dissipation term is the sum of the saturation-based term of Ardhuin et al. (2008a) and the cumulative breaking term $S_{\mathrm{ds,c}}$ of Filipot et al. (2008). It thus takes the form

$$S_{\mathrm{ds}}(f,\theta) = \sigma C_{\mathrm{ds}} \left\{ 0.25 \left[\max\left\{ \frac{B(f)}{B_r} - 1, 0 \right\} \right]^2 + 0.75 \left[\max\left\{ \frac{B'(f,\theta)}{B_r} - 1.0 \right\} \right]^2 \right\} \times F(f,\theta) + S_{\mathrm{ds,c}}(f,\theta), \tag{B10}$$

where

$$B'(f,\theta) = \int_{\theta-80^\circ}^{\theta+80^\circ} k^3 \cos^2(\theta-\theta') F(f,\theta') C_g/(2\pi)\, d\theta', \quad \text{and} \tag{B11}$$

$$B(f) = \max\{B'(f,\theta), \theta \in [0, 2\pi]\}, \tag{B12}$$

and $B_r = 0.0009$ is a threshold for the onset of breaking consistent with the observations of Banner et al. (2000) and Banner et al. (2002), as discussed by Babanin and van der Westhuysen (2008), when including the normalization by the width of the directional spectrum [here replaced by the $\cos^2$ factor in Eq. (B11)]. The dissipation constant C_{ds} was adjusted to 2.2×10^{-4} in order to reproduce the directional fetch-limited data described by Ardhuin et al. (2007).

The cumulative breaking term represents the smoothing of the surface by big breakers with celerity C' that wipes out smaller waves of phase speed C (Babanin and Young 2005). Because of uncertainties in the estimation of this effect from observations, we use the theoretical model of Filipot et al. (2008). Briefly, the relative velocity of the crests is the norm of the vector difference, $\Delta_C = |\mathbf{C} - \mathbf{C}'|$, and the dissipation rate of short wave is simply the rate of passage of the large breaker over short waves [i.e., the integral of $\Delta_C \Lambda(\mathbf{C})\, d\mathbf{C}$, where $\Lambda(\mathbf{C})\, d\mathbf{C}$ is the length of breaking crests per unit surface that have velocity components between C_x and $C_x + dC_x$ and between C_y and $C_y + dC_y$; Phillips 1985]. Because there is no consensus on the form of Λ (Gemmrich et al. 2008), we prefer to link Λ to breaking probabilities. Based on Banner et al. (2000, their Fig. 6) and taking their saturation parameter ϵ to be on the order of $1.6\sqrt{B}$, the breaking probability of dominant waves is approximately $P = 28.4(\max\{\sqrt{B} - \sqrt{B_r}, 0\})^2$. In this expression, a

division by 2 was included to account for the fact that their breaking probabilities were defined for waves detected by using a zero-crossing analysis, which underestimates the number of dominant waves, because at any given time only one wave is present and thus low waves of the dominant scale are not counted when shorter but higher waves are present.

Extrapolating this result to higher frequencies and assuming that the spectral density of crest length per unit surface $l(\mathbf{k})$ in the wavenumber spectral space is $l(\mathbf{k}) = 1/(2\pi^2 k)$, we define a spectral density of breaking crest length, $\Lambda(\mathbf{k}) = l(\mathbf{k})P(\mathbf{k})$, giving the source term,

$$S_{\mathrm{ds,c}}(f,\theta) = -c_3 F(f,\theta)\int_0^{0.7f}\int_0^{2\pi}\frac{56.3}{\pi} \times \max\{\sqrt{B(f',\theta')} - \sqrt{B_r}, 0\}\frac{\Delta_C}{C_g'}\,d\theta'\,df'. \tag{B13}$$

The tuning coefficient c_3, which was expected to be on the order of 1, was adjusted here to 0.4. The resulting model results appear to be very accurate for sea states with significant wave heights up to 8 m. Larger wave heights are underestimated. Other parameter adjustments can correct for this defect (e.g., reducing s_u and increasing c_3), but then the Stokes drift may not be so well reproduced, especially for the average conditions discussed here. These different possible adjustments and their effects will be discussed elsewhere.

b. Numerical schemes and model settings

Spatial advection in the finer model grid is performed using the explicit contour integration based residual distribution–narrow stencil (CRD-N) scheme (Csík et al. 2002) that was applied to the wave action equation by Roland (2009) and provided as a module for the WWIII model. The scheme is first order in time and space, conservative, and monotone.

All model grids are forced by 6-hourly wind analysis at 0.5° resolution provided by ECMWF. The model spectral grid has 24 regularly spaced directions and extends from 0.037 to $f_{\max} = 0.72$ Hz with 32 frequencies exponentially spaced. The model thus covers the full range of frequencies that contribute most to the filtered Stokes drift $\mathbf{U}_{Sf}$. The usual high-frequency tail proportional to f^{-5} is only imposed for frequencies larger than the diagnostic frequency $f_d = Ff_{m,0,-1}$, with the mean frequency defined by $f_{m,0,-1} = [\int E(f)/f\,df/\int E(f)\,df]^{-1}$. Here, we take a factor $F = 10$, instead of the usual value of 2.5 (Bidlot et al. 2007), so that f_d is almost always larger than the model maximum frequency of 0.72 Hz. Besides, the time step for integration of the source function is adaptatively refined from 150 s for the local model down to 10 s if needed, so that virtually no limiter constrains the wave field evolution (Tolman 2002).

APPENDIX C

Model Accuracy for Relevant Parameters

To define the errors on the estimations of U_{Sf} used to determine the quasi-Eulerian velocity U_E from the radar measurement, it is necessary to examine the quality of the wind forcing and model results in the area of interest, as summarized in Table C1. The only two parameters that are measured continuously offshore of the area of interest are the wave height H_s and mean period f_{02}, recorded at buoy 62163, which is 150 km to the west of point A. The values of H_s and f_{02} can be combined to give the second moment of the wave spectrum $m_2 = (0.25H_sf_{02})^2$ (Fig. C1).

Because there is no reliable wave measurement with spectral information in deep water off the northeast French Atlantic coast, we also use buoy data and model results in a relatively similar wave environment, at the location of buoy 46005, which is 650 km off Aberdeen, Washington, on the U.S. Pacific coast. Because this buoy is not directional we first examine the third moment of the wave spectrum:

$$m_3(f_c) = \int_0^{f_c} f^3 E(f)\,df. \tag{C1}$$

If waves were all in the same direction, m_3 would be proportional to the Stokes drift $U_{\mathrm{ss}}(f_c)$ of waves with frequency up to f_c, as given by Eq. (4). We thus define a nondirectional Stokes drift as

$$U_{\mathrm{ssnd}}(f_c) = 2(2\pi)^3 m_3(f_c)/g. \tag{C2}$$

Looking at buoy data, we found that

$$U_{\mathrm{ssnd}}(f_c) \simeq 5.9\times10^{-4}\left[1.25 - 0.25\left(\frac{0.5}{f_c}\right)^{1.3}\right]U_{10} \times \min\{U_{10}, 14.5\} + 0.027(H_s - 0.4), \tag{C3}$$

where f_c is in hertz, U_{10} is in meters per second, and H_s is in meters.

Taking directionality into account, Eq. (4) yields $U_{\mathrm{ss}}(f_c) \simeq 0.85U_{\mathrm{ssnd}}(f_c)$ for typical wave spectra and the relationship (C3) becomes Eq. (7). For buoy 46005, which is a 6-m Navy Oceanographic Meteorological Automatic Device (NOMAD) buoy, and f_c in the range

TABLE C1. Model accuracy for measured wave parameters in various regions of the World Ocean. Buoy validations span the entire year 2007, except for buoy 62069, for which data cover 25 Jan–20 Aug 2008; buoy Iroise, which covers 13 Apr–20 May 2004; and *Jason-1*, for which data correspond to January–July 2007 for the global validation (JAS-Glo: 393 382 data points) and the full year for a box 3° × 4° centered on 48°30′N, 8°W or 45°N, 128°W (JAS-Gas or JAS-Was: 380 data points). Unless otherwise specified by the number in parenthesis, the cut-off frequency is 0.5 Hz, *C* stands for C band, and $f_B = 0.36$ Hz corresponds to our 12-MHz HF radar. The normalized bias (NB) is defined as the bias divided by the rms observed value, whereas the scatter index (SI) is defined as the rms difference between modeled and observed values, after correction for the bias and normalized by the rms observed value, and r is Pearson's correlation coefficient. Only altimeter data are available at point A, but the uniform error pattern and the model consistency suggest that errors at A should be similar to offshore buoy errors such as those found at buoy 62163 offshore of A or at the U.S. West Coast buoy 46005. Errors at point B, not discussed here, are expected to be closer to those at the nearshore buoys 62069 and Iroise.

	Dataset	NB (%)	SI (%)	r
2004				
H_s	62163	6.8	11.1	0.977
f_{02}	62163	10.4	8.8	0.907
H_s	Iroise	12.8	17.4	0.975
f_{02}	Iroise	−10.0	11.7	0.913
$U_{\mathrm{ssnd}}(f_B)$	Iroise	27.2	26.9	0.968
$U_{\mathrm{ss}}(f_B)$	Iroise	20.5	18.5	0.971
2007/08				
H_s	JAS-Glo	−0.6	11.4	0.966
$m_4(C)$	JAS-Glo	0.6	9.1	0.939
H_s	62163	−1.4	8.8	0.985
f_{02}	62163	6.3	7.3	0.938
H_s	62069	10.1	14.1	0.974
f_{02}	62069	−7.7	11.8	0.886
$m_4(f_B)$	62069	15.8	24.1	0.955
$U_{\mathrm{ssnd}}(f_B)$	62069	13.9	23.0	0.965
$U_{\mathrm{ss}}(f_B)$	62069	11.1	21.0	0.963
H_s	JAS-Gas	−2.6	8.8	0.983
$m_4(C)$	JAS-Gas	1.0	6.7	0.962
H_s	46005	4.9	10.2	0.975
f_{02}	46005	−2.8	6.6	0.931
$m_4(f_B)$	46005	−5.4	13.5	0.965
$U_{\mathrm{ssnd}}(f_B)$	46005	−4.9	12.6	0.973
$U_{\mathrm{ss}}(0.5)$	46005	6.2	12.7	0.971
H_s	JAS-Was	2.4	7.9	0.985
$m_4(C)$	JAS-Was	1.8	7.3	0.953

0.3–0.5 Hz, this relationship gives an rms error less than 1.0 cm s^{-1}, which corresponds to less than 15% of the rms value estimated using Eq. (C2). This is smaller than the error of estimates using previous wave models (24% with the parameterization by Bidlot et al. 2007) but comparable to the 14.2% error obtained with the present model. The same analysis was performed, with similar results, for very different sea states recorded by National Data Buoy Center (NDBC) buoys 51001 (northeast of Hawaii), 41002 (U.S. East Coast), 46047 (Tanner Banks, California), and 42036 (Gulf of Mexico).

Another source of continous wave measurements is provided by altimeter-derived H_s, which we correct for bias following Queffeulou (2004), and fourth spectral moment m_4. The latter is approximately given by (Vandemark et al. 2004)

$$m_4 = \frac{0.64g^2}{(2\pi)^4\sigma_0}, \qquad \text{(C4)}$$

where σ_0 is the normalized radar cross section, corrected for a 1.2-dB bias on the C-band altimeter of *Jason* in order to fit airborne observations (Hauser et al. 2008). The model estimation of m_4 (0.72 Hz) is extrapolated to C-band by the addition of a constant $0.011g^2/(2\pi)^4$, which is consistent with the saturation of the short wave slopes observed by Vandemark et al. (2004). For this parameter, the model is found to be very accurate, especially around the region of interest, more accurate than on the U.S. Pacific coast.

These indirect validations suggest that the third spectral moment including waves up to the Bragg frequency $f_B = 0.36$ Hz, which is proportional to U_{ssnd}, is probably estimated with bias between −5% and 10% and an rms error less than 20%. The bias on the significant wave height appears to increase from offshore (altimeter and buoy 62163 data) to the coast (buoys Iroise and 62069), and we attribute this effect to the tidal currents (not included in the present wave model) and

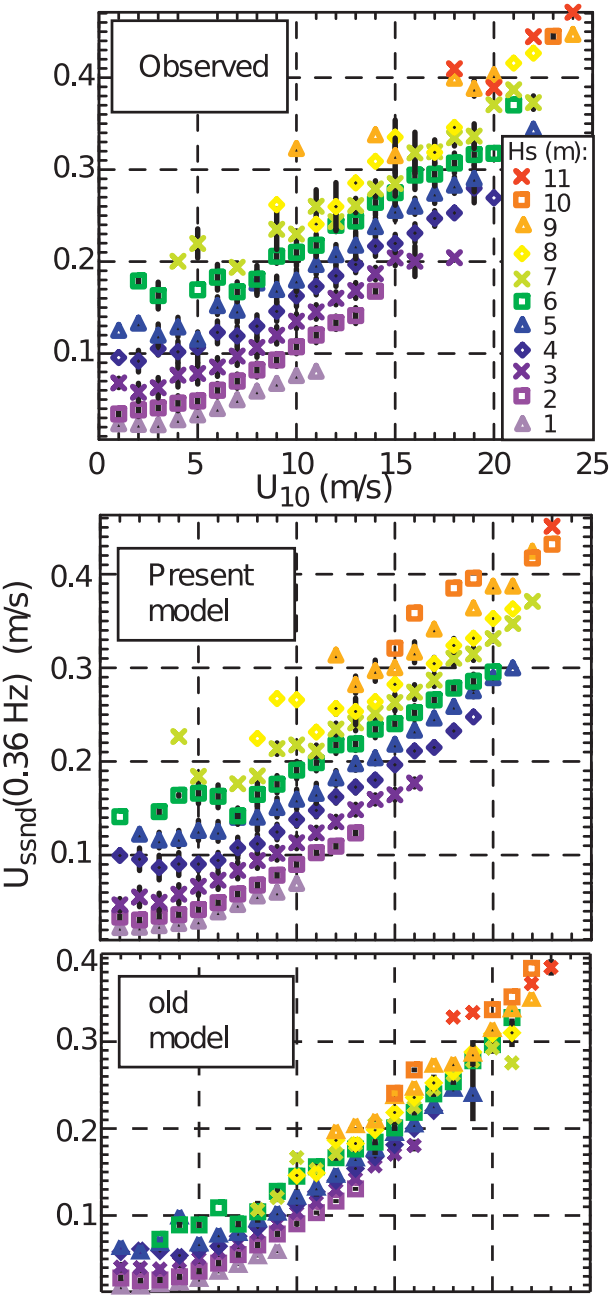

FIG. C1. Variation of the wave spectrum third moment m_3 converted to a velocity $U_{\text{ssnd}} = (2\pi)^3 m_3(f_c)/g$ that would equal the surface Stokes drift in deep water if all waves propagated in the same direction. For each data source, a cut-off frequency of $f_c = f_B =$ 0.36 Hz is taken and the data are binned wind speed at 1 m s^{-1} intervals and significant wave height H_s (in colors) at 1-m intervals from 1 to 11 m. (top) Buoy data offshore of Oregon (NDBC buoy 46005); (middle) present model results; and (bottom) results from the same model but using the parameterization of Bidlot et al. (2007), including a factor $F = 2.5$. The vertical error bars indicate $\pm 1/2$ the standard deviation of the data values in each (U_{10}, H_s) class.

coastal modifications of the winds that are not well reproduced at this 10–20-km scale by the ECMWF model. Because the chosen area of interest lies offshore of the area where currents are strongest (Fig. 1), we shall assume that, at this site, the model bias on $U_{ss}(f_B)$ is zero, which appears most likely. Extreme biases of $\pm 10\%$ only result in deflections of 5° on the diagnosed quasi-Eulerian current U_E.

REFERENCES

Agrawal, Y. C., E. A. Terray, M. A. Donelan, P. A. Hwang, A. J. Williams, W. Drennan, K. Kahma, and S. Kitaigorodskii, 1992: Enhanced dissipation of kinetic energy beneath breaking waves. *Nature,* **359,** 219–220.

Ardhuin, F., 2006: Quelles mesures pour la prévision des états de mer en zone côtiére? [Available online at http://www.ifremer.fr/aei2006/resume_long/T1S3/14-aei2006-55.pdf.]

——, F.-R. Martin-Lauzer, B. Chapron, P. Craneguy, F. Girard-Ardhuin, and T. Elfouhaily, 2004: Dérive à la surface de l'océan sous l'effet des vagues. *Compt. Rend. Géosci.,* **336,** 1121–1130, doi:10.1016/j.crte.2004.04.007.

——, T. H. C. Herbers, K. P. Watts, G. P. van Vledder, R. Jensen, and H. Graber, 2007: Swell and slanting fetch effects on wind wave growth. *J. Phys. Oceanogr.,* **37,** 908–931.

——, F. Collard, B. Chapron, P. Queffeulou, J.-F. Filipot, and M. Hamon, 2008a: Spectral wave dissipation based on observations: A global validation. *Proc. Chinese–German Joint Symp. on Hydraulics and Ocean Engineering,* Darmstadt, Germany, Institut für Wasserbau und Wasserwirtschaft, 391–400.

——, N. Rascle, and K. A. Belibassakis, 2008b: Explicit wave-averaged primitive equations using a generalized Lagrangian mean. *Ocean Modell.,* **20,** 35–60, doi:10.1016/j.ocemod.2007.07.001.

——, B. Chapron, and F. Collard, 2009: Observation of swell dissipation across oceans. *Geophys. Res. Lett.,* **36,** L06607, doi:10.1029/2008GL037030.

Babanin, A. V., and I. R. Young, 2005: Two-phase behaviour of the spectral dissipation of wind waves. *Proc. 5th Int. Symp. Ocean Wave Measurement and Analysis,* Madrid, Spain, ASCE, 11 pp.

——, and A. J. van der Westhuysen, 2008: Physics of saturation-based dissipation functions proposed for wave forecast models. *J. Phys. Oceanogr.,* **38,** 1831–1841.

Banner, M. L., A. V. Babanin, and I. R. Young, 2000: Breaking probability for dominant waves on the sea surface. *J. Phys. Oceanogr.,* **30,** 3145–3160.

——, J. R. Gemmrich, and D. M. Farmer, 2002: Multiscale measurement of ocean wave breaking probability. *J. Phys. Oceanogr.,* **32,** 3364–3374.

Barrick, D. E., and B. L. Weber, 1977: On the nonlinear theory for gravity waves on the ocean's surface. Part II: Interpretation and applications. *J. Phys. Oceanogr.,* **7,** 3–10.

Battjes, J. A., and J. P. F. M. Janssen, 1978: Energy loss and set-up due to breaking of random waves. *Proc. 16th Int. Conf. on Coastal Engineering,* Hamburg, Germany, ASCE, 569–587.

Bidlot, J., P. Janssen, and S. Abdalla, 2007: A revised formulation of ocean wave dissipation and its model impact. Tech. Rep. Memo. 509, ECMWF, 29 pp.

Broche, P., J. C. de Maistre, and P. Forget, 1983: Mesure par radar décamétrique cohérent des courants superficiels engendrés par le vent. *Oceanol. Acta,* **6,** 43–53.

Chapman, R. D., L. K. Shay, H. Graber, J. B. Edson, A. Karachintsev, C. L. Trump, and D. B. Ross, 1997: On the accuracy of HF radar surface current measurements: Intercomparisons with ship-based sensors. *J. Geophys. Res.,* **102,** 18 737–18 748.

Chapron, B., F. Collard, and F. Ardhuin, 2005: Direct measurements of ocean surface velocity from space: Interpretation and validation. *J. Geophys. Res.,* **110,** C07008, doi:10.1029/2004JC002809.

Chen, G., and S. E. Belcher, 2000: Effects of long waves on wind-generated waves. *J. Phys. Oceanogr.,* **30,** 2246–2256.

Craig, P. D., and M. L. Banner, 1994: Modeling wave-enhanced turbulence in the ocean surface layer. *J. Phys. Oceanogr.,* **24,** 2546–2559.

Csík, Á., M. Ricchiuto, and H. Deconinck, 2002: A conservative formulation of the multidimensional upwind residual distribution schemes for general nonlinear conservation laws. *J. Comput. Phys.,* **172,** 286–312.

Davis, R. E., 1985: Drifter observations of coastal currents during CODE: The method and descriptive view. *J. Geophys. Res.,* **90,** 4741–4755.

Dobson, F., W. Perrie, and B. Toulany, 1989: On the deep water fetch laws for wind-generated surface gravity waves. *Atmos.–Ocean,* **27,** 210–236.

Ekman, V. W., 1905: On the influence of the Earth's rotation on ocean currents. *Arch. Math. Astron. Phys.,* **2,** 1–52.

Elipot, S., and R. Lumpkin, 2008: Spectral description of oceanic near-surface variability. *Geophys. Res. Lett.,* **35,** L05606, doi:10.1029/2007GL032874.

Essen, H.-H., 1993: Ekman portions of surface currents, as measured by radar in different areas. *Deutsche Hydrogr. Z.,* **45,** 57–85.

Filipot, J.-F., F. Ardhuin, and A. Babanin, 2008: Paramétrage du déferlement des vagues dans les modèles spectraux: Approches semi-empirique et physique. *Actes des Xèmes Journées Génie Côtier-Génie Civil, Sophia Antipolis,* Centre Français du Littoral, 335–344.

Gemmrich, J. R., M. L. Banner, and C. Garrett, 2008: Spectrally resolved energy dissipation rate and momentum flux of breaking waves. *J. Phys. Oceanogr.,* **38,** 1296–1312.

Gonella, J., 1971: A local study of inertial oscillations in the upper layers of the ocean. *Deep-Sea Res.,* **18,** 776–788.

——, 1972: A rotary-component method for analyzing meteorological and oceanographic vector time series. *Deep-Sea Res.,* **19,** 833–846.

Gourrion, J., D. Vandemark, S. Bailey, and B. Chapron, 2002: Investigation of C-band altimeter cross section dependence on wind speed and sea state. *Can. J. Remote Sens.,* **28,** 484–489.

Grant, W. D., and O. S. Madsen, 1979: Combined wave and current interaction with a rough bottom. *J. Geophys. Res.,* **84,** 1797–1808.

Gurgel, K.-W., and Y. Barbin, 2008: Suppressing radio frequency interference in HF radars. *Sea Technol.,* **49,** 39–42.

——, G. Antonischki, H.-H. Essen, and T. Schlick, 1999: Wellen radar (WERA), a new ground-wave based HF radar for ocean remote sensing. *Coast. Eng.,* **37,** 219–234.

Hackett, B., Ø. Breivik, and C. Wettre, 2006: Forecasting the drift of objects and substances in the ocean. *Ocean Weather Forecasting,* E. P. Chassignet and J. Verron, Eds., Springer, 507–523.

Hasselmann, K., 1970: Wave-driven inertial oscillations. *Geophys. Fluid Dyn.,* **1,** 463–502.

Hasselmann, S., K. Hasselmann, J. Allender, and T. Barnett, 1985: Computation and parameterizations of the nonlinear energy transfer in a gravity-wave spectrum. Part II: Parameterizations of the nonlinear energy transfer for application in wave models. *J. Phys. Oceanogr.,* **15,** 1378–1391.

Hauser, D., G. Caudal, S. Guimbard, and A. A. Mouche, 2008: A study of the slope probability density function of the ocean waves from radar observations. *J. Geophys. Res.,* **113,** C02006, doi:10.1029/2007JC004264.

Huang, N. E., and C.-C. Tung, 1976: The dispersion relation for a nonlinear random gravity wave field. *J. Fluid Mech.,* **75,** 337–345.

Ivonin, D. V., P. Broche, J.-L. Devenon, and V. I. Shrira, 2004: Validation of HF radar probing of the vertical shear of surface currents by acoustic Doppler current profiler measurements. *J. Geophys. Res.,* **101,** C04003, doi:10.1029/2003JC002025.

Janssen, P. A. E. M., 1991: Quasi-linear theory of wind wave generation applied to wave forecasting. *J. Phys. Oceanogr.,* **21,** 1631–1642.

Jenkins, A. D., 1987: Wind and wave induced currents in a rotating sea with depth-varying eddy viscosity. *J. Phys. Oceanogr.,* **17,** 938–951.

Kahma, K. K., and C. J. Calkoen, 1992: Reconciling discrepancies in the observed growth of wind-generated waves. *J. Phys. Oceanogr.,* **22,** 1389–1405.

Kantha, L. H., and C. A. Clayson, 2004: On the effect of surface gravity waves on mixing in the oceanic mixed layer. *Ocean Modell.,* **6,** 101–124.

——, P. Wittmann, M. Sclavo, and S. Carniel, 2009: A preliminary estimate of the Stokes dissipation of wave energy in the global ocean. *Geophys. Res. Lett.,* **36,** L02605, doi:10.1029/2008GL036193.

Kinsman, B., 1965: *Wind Waves*. Prentice-Hall, 676 pp.

Kirby, J. T., and T.-M. Chen, 1989: Surface waves on vertically sheared flows: Approximate dispersion relations. *J. Geophys. Res.,* **94,** 1013–1027.

Kirwan, A. D., Jr., G. McNally, S. Pazan, and R. Wert, 1979: Analysis of surface current response to wind. *J. Phys. Oceanogr.,* **9,** 401–412.

Le Boyer, A., G. Cambon, N. Daniault, S. Herbette, B. L. Cann, L. Marie, and P. Morin, 2009: Observations of the Ushant tidal front in September 2007. *Cont. Shelf Res.,* **29,** 1026–1037, doi:10.1016/j.csr.2008.12.020.

Longuet-Higgins, M. S., and O. M. Phillips, 1962: Phase velocity effects in tertiary wave interactions. *J. Fluid Mech.,* **12,** 333–336.

Madsen, O. S., 1977: A realistic model of the wind-induced Ekman boundary layer. *J. Phys. Oceanogr.,* **7,** 248–255.

Mao, Y., and M. L. Heron, 2008: The influence of fetch on the response of surface currents to wind studied by HF ocean surface radar. *J. Phys. Oceanogr.,* **38,** 1107–1121.

Mariette, V., and B. Le Cann, 1985: Simulation of the formation of the Ushant thermal front. *Cont. Shelf Res.,* **4,** 637.

McWilliams, J. C., P. P. Sullivan, and C.-H. Moeng, 1997: Langmuir turbulence in the ocean. *J. Fluid Mech.,* **334,** 1–30.

Mellor, G., and A. Blumberg, 2004: Wave breaking and ocean surface layer thermal response. *J. Phys. Oceanogr.,* **34,** 693–698.

Millot, C., and M. Crépon, 1981: Inertial oscillations on the continental shelf of the Gulf of Lions—Observations and theory. *J. Phys. Oceanogr.,* **11,** 639–657.

Nerheim, S., and A. Stigebrandt, 2006: On the influence of buoyancy fluxes on wind drift currents. *J. Phys. Oceanogr.,* **36,** 1591–1604.

Pawlowicz, R., B. Beardsley, and S. Lentz, 2002: Classical tidal harmonic analysis including error estimates in MATLAB using T_TIDE. *Comput. Geosci.,* **28,** 929–937.

Phillips, O. M., 1985: Spectral and statistical properties of the equilibrium range in wind-generated gravity waves. *J. Fluid Mech.,* **156,** 505–531.

Pollard, R. T., 1983: Observations of the structure of the upper ocean: Wind-driven momentum budget. *Philos. Trans. Roy. Soc. London,* **A380,** 407–425.

Polton, J. A., D. M. Lewis, and S. E. Belcher, 2005: The role of wave-induced Coriolis–Stokes forcing on the wind-driven mixed layer. *J. Phys. Oceanogr.,* **35,** 444–457.

Prandle, D., 1987: The fine-structure of nearshore tidal and residual circulations revealed by H.F. radar surface current measurements. *J. Phys. Oceanogr.,* **17,** 231–245.

Price, J. F., and M. A. Sundermeyer, 1999: Stratified Ekman layers. *J. Geophys. Res.,* **104,** 20 467–20 494.

Queffeulou, P., 2004: Long term validation of wave height measurements from altimeters. *Mar. Geod.,* **27,** 495–510, doi:10.1080/01490410490883478.

Rascle, N., 2007: Impact of waves on the ocean circulation (in French). Ph.D. thesis, Universite de Bretagne Occidentale. [Available online at http://tel.archives-ouvertes.fr/tel-00182250/.]

——, and F. Ardhuin, 2009: Drift and mixing under the ocean surface revisited. stratified conditions and model-data comparisons. *J. Geophys. Res.,* **114,** C02016, doi:10.1029/2007JC004466.

——, ——, and E. A. Terray, 2006: Drift and mixing under the ocean surface. a coherent one-dimensional description with application to unstratified conditions. *J. Geophys. Res.,* **111,** C03016, doi:10.1029/2005JC003004.

——, ——, P. Queffeulou, and D. Croize-Fillon, 2008: A global wave parameter database for geophysical applications. Part 1: Wave-current–turbulence interaction parameters for the open ocean based on traditional parameterizations. *Ocean Modell.,* **25,** 154–171, doi:10.1016/j.ocemod.2008.07.006.

Rio, M.-H., and F. Hernandez, 2003: High-frequency response of wind-driven currents measured by drifting buoys and altimetry over the world ocean. *J. Geophys. Res.,* **108,** 3283, doi:10.1029/2002JC001655.

Roland, A., 2009: *Development of WWM II: Spectral wave modelling on unstructured meshes.* Ph.D. thesis, Technische Universitat Darmstadt, 212 pp.

Santala, M. J., and E. A. Terray, 1992: A technique for making unbiased estimates of current shear from a wave-follower. *Deep-Sea Res.,* **39,** 607–622.

Shay, L. K., J. Martinez-Pedraja, T. M. Cook, and B. K. Haus, 2007: High-frequency radar mapping of surface currents using WERA. *J. Atmos. Oceanic Technol.,* **24,** 484–503.

Smith, J. A., 2006: Wave-current interactions in finite-depth. *J. Phys. Oceanogr.,* **36,** 1403–1419.

Stewart, R. H., and J. W. Joy, 1974: HF radio measurements of surface currents. *Deep-Sea Res.,* **21,** 1039–1049.

Terray, E. A., M. A. Donelan, Y. C. Agrawal, W. M. Drennan, K. K. Kahma, A. J. Williams, P. A. Hwang, and S. A. Kitaigorodskii, 1996: Estimates of kinetic energy dissipation under breaking waves. *J. Phys. Oceanogr.,* **26,** 792–807.

Tolman, H. L., 2002: Limiters in third-generation wind wave models. *Global Atmos. Ocean Sys.,* **8,** 67–83.

——, 2007: The 2007 release of WAVEWATCH III. *Proc. 10th Int. Workshop of Wave Hindcasting and Forecasting,* Oahu, HI, U.S. Army Engineer Research and Development Center's Coastal and Hydraulics Laboratory, 12 pp. [Available online at http://www.waveworkshop.org/10thWaves/Papers/oahu07_Q4.pdf.]

——, 2008: A mosaic approach to wind wave modeling. *Ocean Modelling,* **25,** 35–47, doi:10.1016/j.ocemod.2008.06.005.

Vandemark, D., B. Chapron, J. Sun, G. H. Crescenti, and H. C. Graber, 2004: Ocean wave slope observations using radar backscatter and laser altimeters. *J. Phys. Oceanogr.,* **34,** 2825–2842.

Wang, W., and R. X. Huang, 2004: Wind energy input to the surface waves. *J. Phys. Oceanogr.,* **34,** 1276–1280.

Weber, B. L., and D. E. Barrick, 1977: On the nonlinear theory for gravity waves on the ocean's surface. Part I: Derivations. *J. Phys. Oceanogr.,* **7,** 3–10.

Xu, Z., and A. J. Bowen, 1994: Wave- and wind-driven flow in water of finite depth. *J. Phys. Oceanogr.,* **24,** 1850–1866.